Schweizerische Eidgenossenschaft
Confédération suisse
Confederazione Svizzera
Confederaziun svizra

Federal Department of the Environment,
Transport, Energy and Communication DETEC

Swiss Federal Office of Energy SFOE
Energy Research and Cleantech

Final report dated 31 May 2019

V-GPER

Industrial validation of the prediction of hydroabrasive erosion of prototype-scale Pelton turbines to reduce the outage time for repair

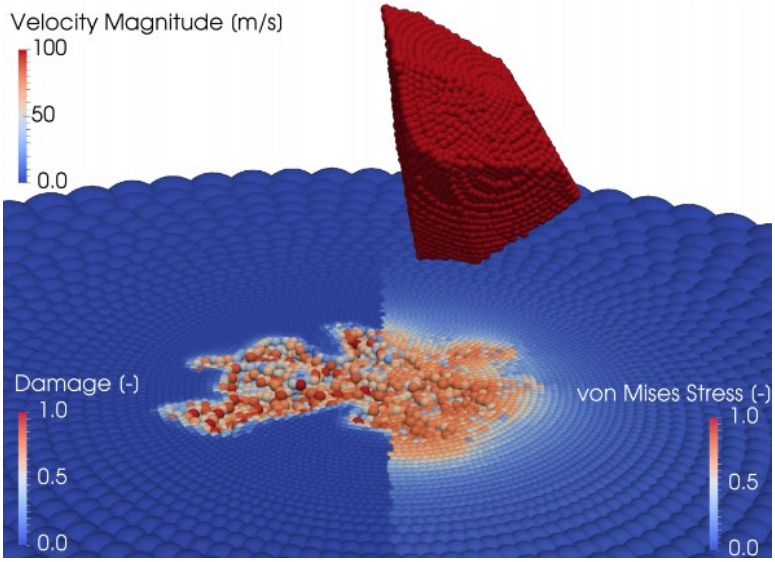

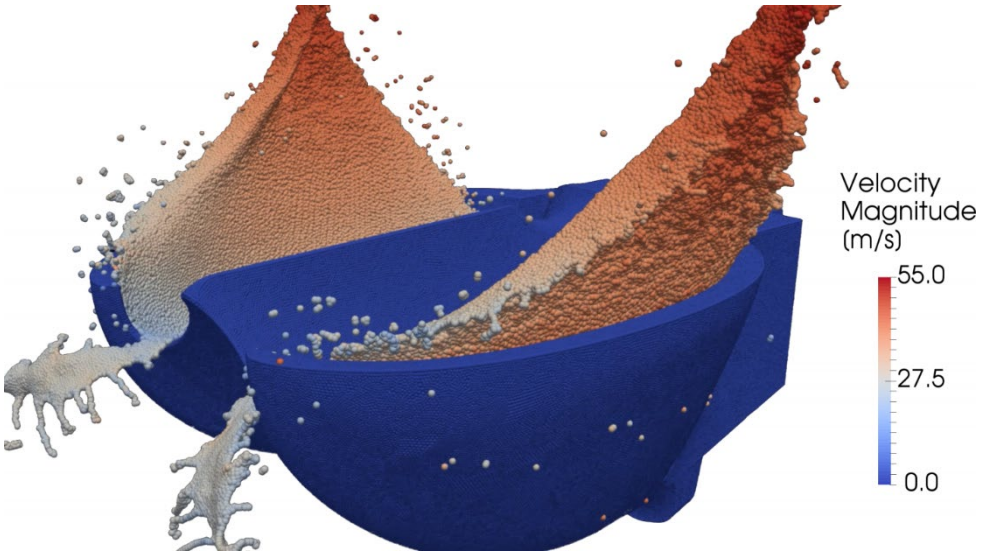

Date: May 31, 2019

Location: Bern

Subsidiser:
Swiss Federal Office of Energy SFOE
Energy Research and Cleantech Section
CH-3003 Bern
www.bfe.admin.ch

Subsidy recipient:
EPFL - Laboratory for Hydraulic Machines (LMH)
Avenue de Cour 33 Bis
CH-1007 Lausanne
https://lmh.epfl.ch/main

Authors:
François Avellan, EPFL-LMH, francois.avellan@epfl.ch
Sebastián Leguizamón, EPFL-LMH, sebastian.legui@epfl.ch
Siamak Alimirzazadeh, EPFL-LMH, siamak.alimirzazadeh@epfl.ch

SFOE project coordinator:
Klaus Jorde, klaus.jorde@kjconsult.net

SFOE contract number: SI/501786-01

Summary

The technical capability to predict the hydroabrasive erosion experienced by a Pelton turbine when operating with sediment-laden flow is a prerequisite for reducing the outage time for repairs. A multiscale numerical methodology to simulate this erosion process has already been validated for laboratory-scale impinging slurry jets on a flat plate, providing unprecedented accuracy. The present project aims at validating the methodology in the industrial environment by performing multiscale simulations of the erosion of prototype-scale Pelton turbines and comparing the results with available experimental data.

The report is related to the numerical simulation of erosion in the two case studies scheduled for the project, i.e. the study case of a Pelton runner bucket at stand still and the study case of rotating runner buckets. The numerical simulation results, such as the sediment flux or the average impact angle and velocity distributions on the bucket surface, bring insight into the erosion process. Furthermore, they explain the resulting erosion distributions, which are in very good agreement with the corresponding experimental erosion results available.

Résumé

La capacité technique permettant la prédiction de l'érosion hydroabrasive d'une turbine Pelton exploitée avec une eau chargée en sédiments est indispensable pour réduire les temps d'arrêts dus aux réparations. Une méthodologie numérique multi-échelle de prédiction a déjà été validée avec une précision inédite à l'échelle du laboratoire dans le cadre d'une étude expérimentale de l'érosion d'une plaque plane par un jet chargé en sédiments. Ce projet consiste à valider cette méthodologie en l'environnement industriel en prédisant l'érosion de turbines Pelton existantes, et comparant les résultats avec des données expérimentales.

Le présent rapport est relatif aux simulations numériques de l'érosion dans les deux cas d'études prévus dans le projet soit le cas d'un auget d'une roue Pelton stationnaire, et le cas d'augets d'une roue Pelton en rotation. Les résultats obtenus tels que les distributions de flux de sédiments, de vitesse et d'angle d'impact sur la paroi de l'auget, apportent un aperçu inédit sur le processus d'érosion. En outre, ils permettent d'expliquer les distributions d'érosion obtenues, qui sont en très bon accord avec les données expérimentales correspondantes.

Main Findings

- The proposed predictive numerical simulation methodology has been demonstrated in a realistic industrial environment;
- The successful validation of the erosion prediction methodology with respect to corresponding experimental data builds confidence on its future use.

Seite absichtlich frei

Contents

List of Abbreviations

CPU	Central Processing Unit
CSCS	Swiss National Supercomputing Centre
EPFL	École polytechnique fédérale de Lausanne
FVPM	Finite Volume Particle Method
GPU	Graphics Processing Unit
LMH	Laboratory for Hydraulic Machines
SFOE	Swiss Federal Office of Energy

1 Introduction

1.1 Background Information and State-of-the-Art

Hydroabrasive erosion is defined as the gradual removal of material from a surface in contact with a sediment-laden flow. The hydroabrasive erosion of hydraulic turbines, especially Pelton buckets, injector needles and nozzles, is a widespread problem that entails efficiency degradation, cavitation enhancement, and outage for expensive repairs (Grein & Schachenmann 1992, Chitrakar et al. 2016). Several erosion mitigation strategies are used in the design and operation of these machines, for example: the use of surface coatings, an ad hoc turbine geometry such as oversized buckets, strategic shutdown in periods of high sediment concentration, periodic welding repairs, and so on (Felix et al. 2016). However, to find the best compromise among these mitigation strategies, it is desirable to have a predictive tool to estimate the erosion damage a turbine will experience under given conditions. With this technical capacity to predict, it would be possible to optimize the turbine design, its operation and maintenance, in view of objectives such as decreasing the outage time and the efficiency degradation.

The experimental investigation of the erosion phenomenon spans six decades (Finnie 1960, Finnie 1972, Shewmon & Sundararajan 1983), and has provided important insight into the mechanisms involved, as well as series of analytical models that are used to date in many empirical erosion correlations. Apart from the general descriptions of the erosion in hydraulic machines (Grein & Schachenmann 1992, Rai et al. 2017), the specificities involved in the erosion process have also been studied, such as the erosion resistance of several martensitic steels and coatings (Mann & Arya 2001), or the mechanisms involved in the erosion of a model Pelton turbine (Padhy & Saini 2012). However, it proves difficult to use these results to predict the erosion of a real machine, partly because of the lack of similarity between the laboratory and prototype conditions. Although empirical models can be calibrated using field data from a specific power plant as recently done by Felix et al. (2016), their transposition remains a problem.

Numerical simulation offers a complementary way of studying the erosion phenomenon. Two different approaches have been used so far. On the first approach, detailed simulations of the sediment impacts have been performed with both finite element methods (Wang & Yang 2008, Balu et al. 2013) and smoothed particle hydrodynamics (Wang & Yang 2009, Takaffoli & Papini 2012); Although limited to a microscopic scale, the advantage of this approach is the use of comprehensive physical models for the erosion process. On the second approach, computational fluid dynamics has been used to track the sediment trajectories through a macroscopic flow domain in steady-state, together with empirical correlations to estimate the erosion caused by each single impact (Wang et al. 2009, Grewal et al. 2015). The advantage of this approach is that it lends itself to realistic conditions such as a variety of sediment sizes, and impact angle and impact velocity distributions over large surfaces. Unfortunately, the use of erosion correlations instead of material modeling significantly decreases the prediction quality of this approach (Messa & Malavasi 2017).

1.2 Project Purpose and Objectives

The main motivation of the V-GPER project is the need to bridge the technical gap in the prediction of the erosion of hydraulic turbines. Hydroabrasive erosion is a widespread problem that is bound to increase in the coming decades as a consequence of glacier retreat in the Alps and elsewhere, which will increase the sediment concentration in the hydro resources. Even though erosion mitigation strategies exist, it is difficult to assess what is the optimum configuration for a given site, in view of the different costs and expected benefits of each option. The aforementioned predictive capability would be

very beneficial for the optimum design and operation of hydro turbines exposed to hydroabrasive erosion.

The main objective of this project is to demonstrate the technical capacity to predict the erosion of industrial-scale Pelton turbines. This technical capacity is provided by a novel multiscale numerical simulation methodology that has already been demonstrated at laboratory scale (Leguizamón et al. 2017) in the context of the CTI project N° 17568.1 PFEN-IW.

Specific objectives to be achieved by the project are as follows:

- Formulate two representative test cases to be used in the model validation;
- Perform the multiscale simulations in the Swiss National Supercomputing Centre (CSCS);
- Validate the results with experimental data;
- Draw conclusions concerning the applicability of the proposed multiscale model.

2 Modeling Methodology

Recently, a multiscale model of erosion has been proposed (Leguizamón et al. 2017). In line with the multiscale character of the hydroabrasive erosion phenomenon, the multiscale model combines the two numerical approaches described above; it has been shown to provide improved accuracy compared to the state-of-the-art erosion models based on empirical correlations. A full description of the physical models employed is not within the scope of this report; only a short description will be provided here since all the details can be found in the aforementioned reference.

2.1 Multiscale Model of Erosion

2.1.1 Microscale Model: Sediment Impacts

In the microscale model, we perform detailed simulations of the sediment impacts and the resulting material damage and removal, instead of relying on empirical erosion correlations to estimate the amount of mass removed by a given impact.

The mass and linear momentum conservation laws are solved for the sediments and the base material, referred to hereafter as the solid. Both materials are modelled as homogeneous and isotropic, together with the temperature-corrected Mie-Grüneisen equation of state to close the system. Whereas the sediments are modelled as elastic, the solid is modelled as elastoplastic by means of the Johnson-Cook strength and damage models (Johnson & Cook 1985), which define the yield stress and failure plastic strain as functions of the strain, strain-rate, temperature and triaxiality states, as studied in Leguizamón et al. (2016). The material frictional and thermoplastic heating are also considered.

2.1.2 Macroscale Model: Turbulent Sediment Transport

In the macroscale model, the turbulent sediment transport, the impact detection between wall and sediments, and the accumulation of eroded mass are calculated on the domain.

The mass and linear momentum conservation laws are solved for the fluid, which is modelled as Newtonian and weakly compressible; The Tait equation of state and the standard k-ε turbulence model with wall function are used for closure. The sediments, considered as point masses, are tracked on-the-fly through the domain using a one-way coupling scheme. The hydrodynamic force on the sediments considers the effect of drag, added mass and pressure gradient. The important effect of turbulence on

the sediment dispersion is considered via a continuous random walk model based on the Langevin equation (Dehbi 2008).

2.1.3 Sequential Multiscale Coupling Strategy

The models are coupled in a sequential manner. First, the space of possible impact conditions is explored by independent microscale simulations, each of which involves about 60 impacts at constant angle and velocity on a microscopic solid block. These simulations render the restitution coefficients and the steady-state erosion ratio (mass eroded/sediment mass) for each impact condition.

Second, the macroscale sediment transport simulation on the domain of interest is performed; every time an impact against the wall is detected, the microscale simulation results are interpolated to determine the sediment rebound velocity (using the restitution coefficients) and the amount of mass removed (using the steady-state erosion ratio and the sediment mass). The impact conditions and the amount of eroded mass are stored at each impact location, so at the end of the macroscale simulation the distributions of eroded mass, erodent mass, impact angle and impact velocity are collected for the wall surface of interest.

2.2 The Finite Volume Particle Method

The governing equations are discretized using the finite volume particle method (FVPM), which is a generalization of the classical finite volume method that consists of overlapping spherical volumes, *i.e.* particles. FVPM is based on an arbitrary Lagrangian-Eulerian formulation, allowing the computational nodes to move with an arbitrary velocity. This flexibility results in a suitable description of moving interfaces, such as a fluid free surface or an erodible solid.

2.2.1 GPU-SPHEROS

In the context of this project, all the simulations are performed with GPU-SPHEROS, which is an in-house implementation of FVPM accelerated on GPUs. GPU-SPHEROS is almost six times faster than the CPU version on a single NVIDIA® TESLA™ P100-SXM2 16GB compared to a CPU node equipped with two Intel® Xeon® E5-2690 V4 Broadwell CPUs. A detailed derivation of the 3D-FVPM formulation, the GPU-accelerated implementation, several validation cases and applications are available in the literature (Jahanbakhsh et al. 2016, Vessaz et al. 2015, Leguizamón et al. 2016, Jahanbakhsh et al. 2017, Alimirzazadeh et al. 2018, Alimirzazadeh et al. 2018).

3 Test Cases and Results

3.1 Description of the Test Cases

With the objective of demonstrating its applicability to realistic industrial-scale problems, the multiscale model is used to simulate the erosion of two prototype-scale Pelton runner buckets impinged by a water jet with sediments.

3.1.1 Test Case 1

The Test Case 1 corresponds to a stationary bucket setup. The test case closely follows the experimental case reported in Rai et al. (2017), which involves the Toss hydro power plant in the Himalayan region of India, featuring medium-sized Pelton turbines. Since it was not possible to obtain the bucket geometry, we used the design reported by Perrig (2007), scaled to exactly match the dimensions of the experimental counterpart.

Given that the simulated bucket is stand still, the experimental relative velocity between the jet and the bucket is used for the simulated jet velocity, namely 28.5 $m \cdot s^{-1}$. The bucket width is 0.38 m, the turbine pitch diameter is 1.09 m, whereas the jet diameter is 0.14 m.

The sediment diameters are randomly drawn from the average size distribution reported in the field study and distributed uniformly in the water volume following a concentration representative of the experimental condition, resulting in a total of about 0.98×10^6 sediment particles.

The FVPM discretization used in Test Case 1 are presented in Figure 1. On the left, the microscale model where the sediment impacts occur is presented, and on the right, the macroscale model, where the turbulent sediment transport by the flow is simulated, is illustrated.

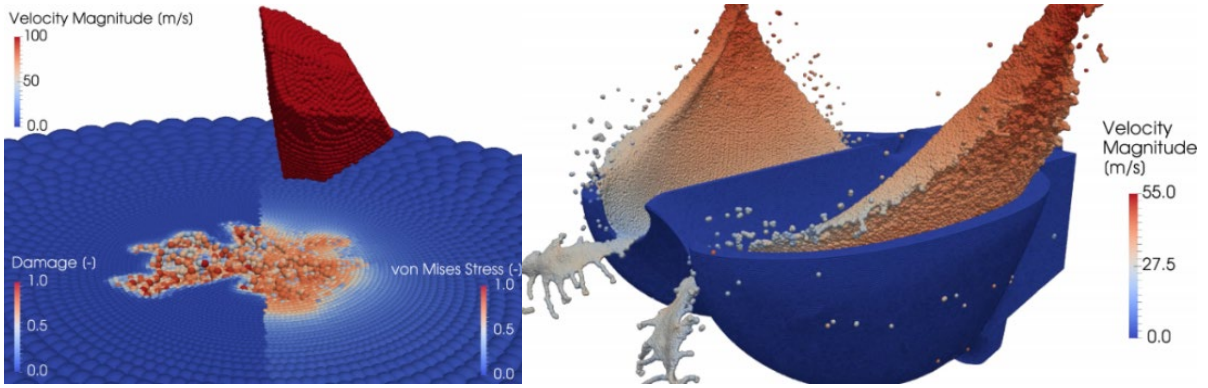

Figure 1: Microscale model simulation of a sharp sediment impacting the solid specimen (left); the solid is colored according to the damage and residual stress caused by previous impacts, whereas the sediment is colored according to its velocity magnitude. Macroscale model simulation of the turbulent flow exiting a prototype-scale stationary Pelton bucket (right); the fluid is coloured according to its velocity magnitude, whereas the sediments are too small to be visible.

3.1.2 Test Case 2

The Test Case 2 corresponds to a Pelton runner in operation for which the field measurements performed by General Electric Renewable Energy at a hydroelectric plant located in the Himalayas are made available. Each runner is characterized by a pitch diameter of 2.87 m and 21 buckets of 0.786 m in width. The rated discharge and head values are 21.9 $m^3 \cdot s^{-1}$ and 435 m, respectively, for a rated power of 84 MW and a jet velocity of 90.20 $m \cdot s^{-1}$. A study period of 21 months comprising 12,114 hours of operation is considered. The sediment concentration was measured by taking periodic samples of the water downstream of the turbines in the tailrace channel and weighting the sediment content. These samples were taken every week for 12 months; in the simulations it is assumed that these measured values are also representative of the corresponding month on the following year (a total of 21 months).

The experimental erosion data were measured using templates along four sections, as illustrated in Figure 2. The experimental erosion depth is available at 4 points on each of the 4 sections, for each one of the buckets. An average erosion depth along each section is also available, as well as an estimation of the total eroded mass.

The macroscale simulation computing domain, also illustrated in Figure 2, includes one jet and three rotating buckets: the first and third buckets are necessary to ensure that the interaction between the jet and the middle one is representative of steady-state turbine operation. As such, only the erosion results of the middle bucket are considered.

A total of 2.25 × 10^6 FVPM particles are used for the simulations including 0.93×10^6 sediments. The sediment diameters are randomly drawn from the average experimental size distribution and distributed uniformly in the water volume according to a concentration representative of the field study. The resulting microscale and macroscale models are like the ones presented in Figure 1 for Test Case 1.

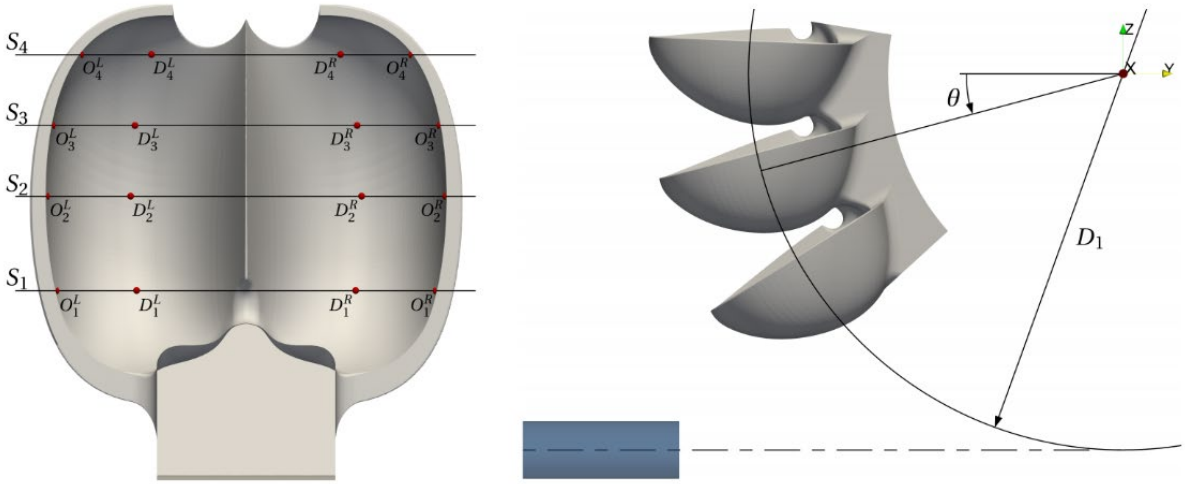

Figure 2: Distribution of the erosion depth measurement points on the bucket surface (left); sketch of the macroscale simulation computational domain (right).

3.2 Results for Test Case 1: Stationary Pelton Bucket

3.2.1 Distributions of Impact Conditions on the Bucket Wall Surface

The results of the average sediment impact velocity and angle on the bucket wall surface and on a slice corresponding to the pitch diameter position are presented in Figure 3.

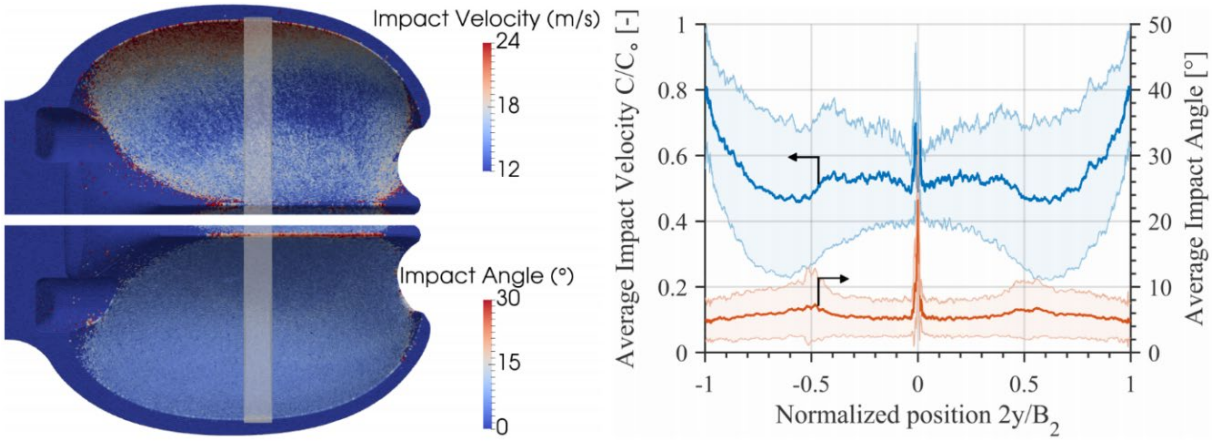

Figure 3: Average impact velocity and angle distributions on the bucket surface (left) and along the pitch diameter position (right). The values on the right represent the average values along the rectangular stripe on the left, which corresponds to the pitch diameter position.

The impact velocity is about 0.5 times the jet velocity $C_\circ$ exactly at the splitter center due to the acceleration experienced by the sediments in the low-velocity stagnation zone, although on the splitter

edges it is as high as 0.7 × $C_\circ$. Throughout most of the bucket the impact velocity is about 0.5 × $C_\circ$, with increasing values towards the bucket outlet, reaching the maximum average impact velocity of 0.8 × $C_\circ$. Furthermore, the average impact angle is fairly uniform throughout the bucket with a value of about 5°, except for the splitter where the impacts occur at about 25°. The fact that the sediments do not impact at higher angles on the splitter indicates that they are responsive to the flow acceleration. These impact condition results are very similar to the 2-D results (Leguizamón et al. 2018) of the same test case.

3.2.2 Distributions of Erosion on the Bucket Surface

The distribution of erodent mass that has impacted the bucket wall and eroded mass of the bucket surface on both the bucket wall and on a slice corresponding to the pitch diameter position are presented in Figure 4. The distribution of erodent mass reveals that most of the sediment impacts occurs on the bucket depth, which corresponds to the zone of maximum bucket curvature. These results highlight the fact that one of the driving mechanisms for sediment flux against the wall, the sediment inertia, is directly linked to the surface curvature. The second hot spot for sediment impacts is the bucket splitter. The sum of erodent mass impacted on the surface is equal to 2.66 times the sum of sediment mass injected, highlighting the fact that sediments tend to impact several times.

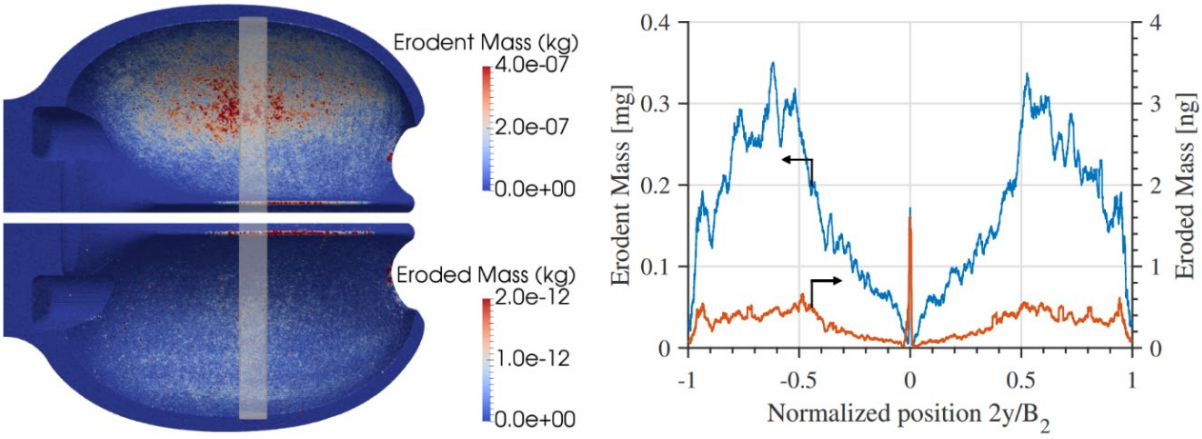

Figure 4: Erodent mass impacted and eroded mass on the bucket surface (left) and along the pitch diameter position (right), which corresponds to the highlighted rectangle on the left.

The superposition of the distributions, *i.e.* where the sediments tend to impact and at what angle and velocity, determines the distribution of eroded mass presented in Figure 4. The amount of eroded mass per unit area has a peak at the splitter, and almost vanished immediately downstream; it gradually increases again towards the bucket outlet. Importantly, note that the distribution of erosion does not only depend on the sediment flux against the wall: even though the erodent mass impacted is greatest at the bucket depth, the eroded mass is greatest at the splitter because of the higher average impact angle at that location. Similarly, despite the relatively low erodent mass impacted towards the bucket outlet, the eroded mass is maintained due to the higher impact velocity at that location. Yet again, these results are very similar to the 2-D results (Leguizamón et al. 2018) of the same test case.

The global erosion ratio computed is equal to 4.04 mg·kg^{-1}. In other words, at these sediment and hydrodynamic conditions, the bucket losses about 4 kg of material for every 1×10^6 kg of sediment that cross it. According to the following validation, this value predicted by the multiscale simulation is quite near its experimental counterpart.

3.2.3 Validation of the Erosion Depth Prediction

We estimate the long-term erosion distribution by extrapolating the simulation results obtained in the original bucket, excluding the surface alteration induced by the process. Note that the incubation period, *i.e.* the initial delay in erosion due to the preliminary accumulation of damage on the surface, is considered in the microscale model by performing enough sediment impacts to reach the steady-state erosion ratio; what is being neglected in the extrapolation is the effect of the macroscopic surface alteration (wavy pattern, roughness) and the resulting modification of the hydrodynamics and therefore of the erosion rate.

The eroded mass distribution presented in Figure 4, which is the consequence of 3.43 g of sediments, is linearly extrapolated to the time frame of the field study, where 737.7×10^3 kg of sediments has crossed the bucket. The extrapolated eroded mass, together with the known material density and surface area per FVPM particle, is used to calculate the distribution of erosion depth after 3180 hours of operation, corresponding to the aforementioned field study time frame.

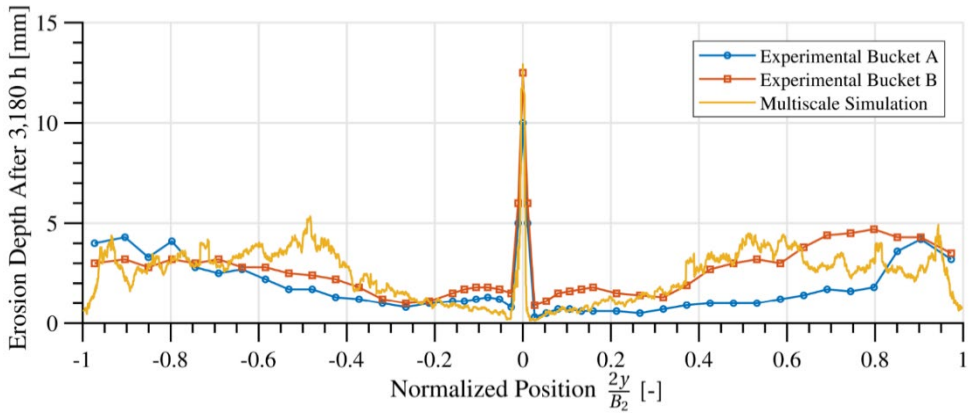

Figure 5: Erosion depth distribution along the pitch diameter position after 3180 hours of operation. The multiscale simulation results compare well with the corresponding experimental data of Rai et al. (2017).

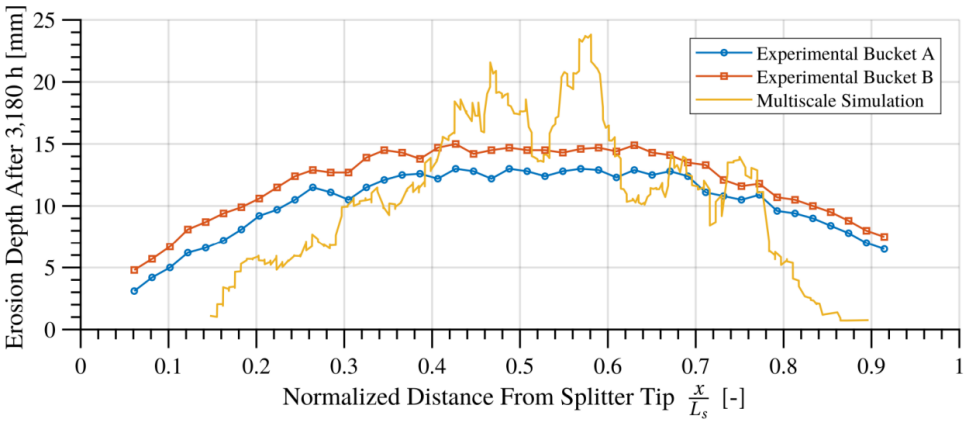

Figure 6: Erosion depth distribution along the splitter after 3180 hours of operation, including the experimental data of Rai et al. (2017).

The multiscale simulation prediction of the erosion depth distribution on the pitch diameter position after 3180 hours of operation, as well as the corresponding measurements reported by Rai et al. (2017) on

two different buckets, are presented in Figure 5. The remarkable agreement between the simulation and the experiment is highlighted, considering the complexity and astounding range of time and length scales involved. Notice that the differences between the two experimental buckets and even between the two sides of each bucket is of comparable magnitude to the difference between the experimental data and the simulation results.

The multiscale simulation prediction of the erosion depth distribution on the bucket splitter is presented in Figure 6, together with the corresponding measurements reported by Rai et al. (2017). Whereas the experimental erosion is widely distributed along the splitter, the simulated erosion is concentrated towards its center. Indeed, as the experimental bucket rotates, the jet is impinging the bucket splitter all along, whereas in the simulated stationary bucket, the jet is impinging only the bucket splitter center. Apart from this discrepancy and the overall lack of smoothness evidenced in the simulated erosion depth, consequence of the short simulation duration, the results agree to a significant extent.

3.3 Results for Test Case 2: Rotating Pelton Runner

3.3.1 Distributions of Impact Conditions on the Bucket Surface

The average impact angle and velocity distributions on the bucket surface are presented in Figure 7. The average impact velocity is about 0.35 × *W* exactly at the splitter center, where *W* is the relative flow velocity with respect to the bucket motion. The low velocity stagnation zone accelerates the sediments, explaining their relatively low impact velocity. The stagnation zone, characterized by high pressure, also deviates some sediments that end up impacting the splitter edges at up to 0.8 × *W*, the highest average impact velocity found. There is a gradual reduction of the impact velocity further downstream, reaching its minimum value of about 0.3 × *W* on the deepest part of the bucket; it gradually increases again towards the outlet, where it reaches 0.5 × *W*. The impact velocity standard deviation is quite uniform and equal to about 0.12 × *W*.

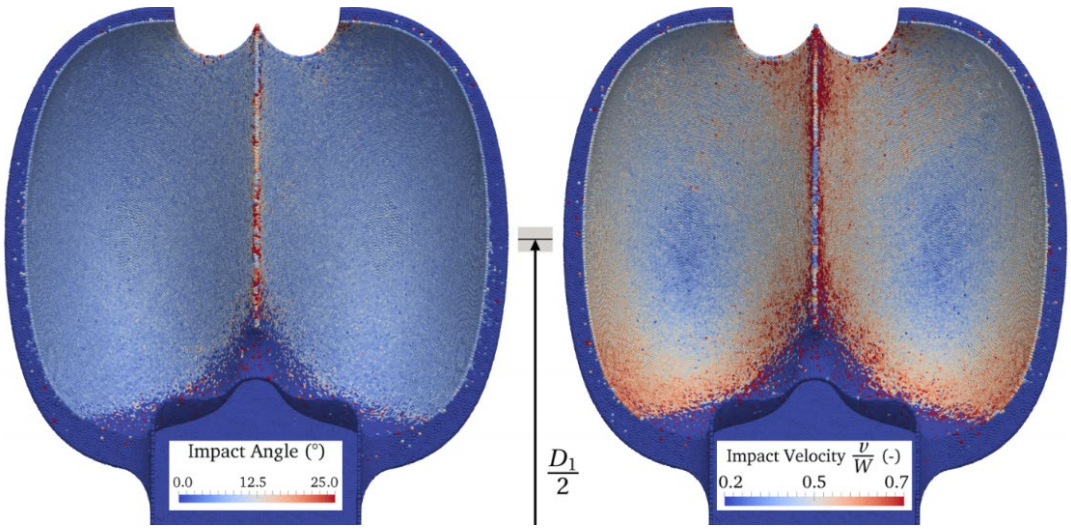

Figure 7: Spatial distributions on the bucket surface of the average impact angle (right) and average impact velocity (left).

The average impact angle is almost uniform and equal to 6° throughout the bucket wall, except at the splitter where it reaches 25°. These low impact angle values highlight the strong influence that the flow

has on the sediment dynamics, preventing impacts at normal incidence. The standard deviation is about 5° throughout most of the bucket, although it reaches 15° at the splitter.

The distributions of impact angle and velocity are comparable to the results of Test Case 1, but not quite equal, suggesting that the model is sensitive enough to discriminate the erosion differences caused by the variation of the bucket geometry, the hydrodynamic conditions, and the sediment characteristics.

3.3.2 Distributions of Erosion on the Bucket Surface

The distribution of impacted erodent mass on the bucket surface is presented in Figure 8. The highest sediment flux occurs at both the bucket splitter and bucket cutout, the places where the fluid experiences the highest acceleration; the sediments therefore separate from the fluid streamlines and have a higher chance of impacting the bucket. Similarly, but to a lower extent, the high-curvature bucket depth is also characterized by a high erodent flux. The sum of erodent mass that impacted the bucket is equal to 4.35 times the total sediment mass that crossed it, *i.e.* sediments tend to impact several times along their trajectory through the bucket. This value is 64 % greater than the one computed in Test Case 1. Dimensional analysis shows that the ratio of centrifugal to drag force experienced by a sediment, which approximates the likelihood of sediment impacts, is proportional to the sediment size and inversely proportional to the bucket size; according to this analysis, the aforementioned ratio of erodent mass impacted to erodent mass injected should be about 50 % greater than for Test Case 1, a trend confirmed by the numerical simulation results.

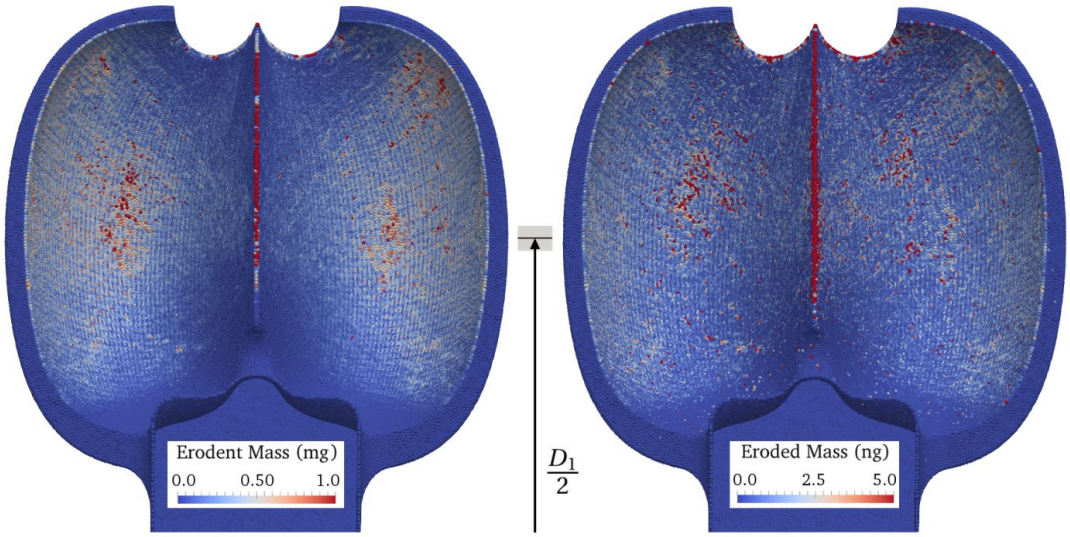

Figure 8: Distributions on the bucket surface of the erodent mass impacted (left) and the eroded mass (right).

The distribution of eroded mass on the bucket surface, also presented in Figure 8, makes apparent the interaction among the distributions of impact conditions and sediment flux. It is maximum at the bucket splitter tip and at the bucket cutout, followed by the bucket bottom, in approximate correspondence with the sediment flux distribution. However, the eroded mass on the bucket bottom is not as high as the erodent mass would indicate due to the relatively low impact velocity in that zone; on the contrary, it increases slightly towards the bucket wall outlet, unlike the sediment flux, due to a local increase of the impact velocity. The eroded mass on the bucket splitter is higher than the erodent mass would suggest due to the relatively high average impact angle on that location.

The ratio between the sum of eroded mass on the bucket and the total sediment mass that crossed it, *i.e.* the global erosion ratio, is equal to 13.02 mg·kg^{-1}. In other words, for the sediment characteristics and hydrodynamic conditions studied, this specific bucket design loses about 13 kg of material for every 1 × 10^6 kg of sediment that crossed the bucket. As demonstrated in the following section, this prediction is in very good agreement with the experimental data available. The global erosion ratio is 222 % higher than for Test Case 1; this difference is mostly explained by the greater relative flow velocity W, which is 58% higher, and correspondingly higher average impact velocities.

3.3.3 Validation of the Erosion Depth Prediction

Like Test Case 1, the simulation results are extrapolated to the time frame of the field study by means of the sediment load ratio between numerical simulations and the field. The eroded mass distribution presented in Figure 8, which corresponds to a total of 5.345 g of sediment, is extrapolated to match the experimental sediment load per bucket, equal to 1.27 × 10^6 kg of sediment; the extrapolated eroded mass is then used to compute a distribution of erosion depth that is compared with the corresponding experimental measurements.

As seen in Figure 9, the standard deviation of both the numerical and the experimental erosion depth results is significant and comparable in magnitude; however, its origin is different for each case. For the experiment, the standard deviation is a measure of the results variability among the samples that constitute each point, *i.e.* the erosion depth irregularity under nominally identical conditions. For the case of the simulation, the standard deviation is a measure of the numerical results variability around each sample point, *i.e.* the noise, a consequence of the short simulation duration and therefore the relatively low number of sediment impacts.

There is a considerable overlap between the simulation predictions and the corresponding experimental results, although the difference of mean values is significant. The erosion depth is underpredicted on the bucket depth, especially at points D_1 and D_4, whereas at the bucket outlet it is rather well predicted. The average relative error of these eight pointwise comparisons is 35%.

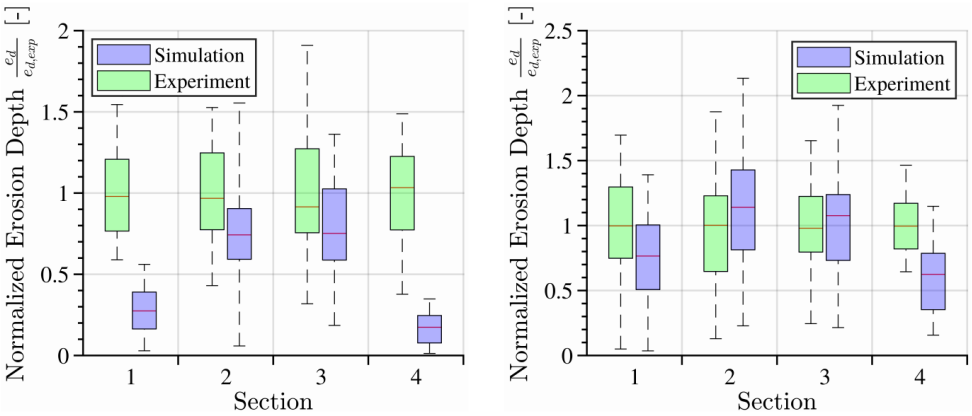

Figure 9: Erosion depth e_d at eight points on the bucket surface, normalized by the corresponding average experimental measurements $e_{d,exp}$. Four points D_i on the bucket depth (left) and four points O_i at its outlet (right), corresponding to the four measurement sections illustrated in Figure 2, are presented. The red lines, lower and upper box bounds, and whiskers represent the median, 25th and 75th percentiles, and extreme values, respectively.

The average erosion depth along each of the four sections shown in Figure 2 is presented in Figure 10, where both the experimental measurements and the multiscale simulation results are normalized by the corresponding average experimental values. Here again a significant spread of the results is evidenced,

as well as an important overlap of experimental and numerical results. The average relative error, calculated using the mean values, is only 14.3%, similar to the standard deviation of the experimental results. This comparison is more forgiving than the preceding pointwise comparison thanks to the cancellation of errors that occurs in the one-dimensional averaging procedure.

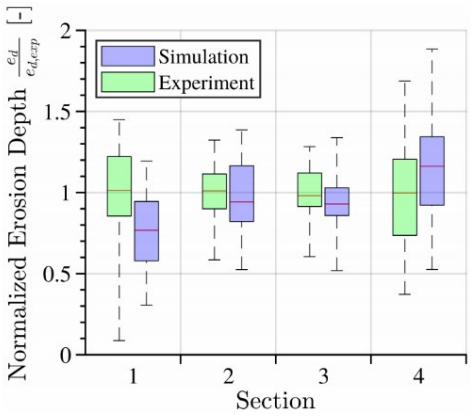

Figure 10: Average erosion depth e_d along the four measurement sections illustrated in Figure 2, normalized by the corresponding average experimental measurements $e_{d,exp}$. See the box plot description in the caption of Figure 9.

The experimental and numerical results for the total eroded mass are compiled in Table 1; the relative error is only 3.9%. Given that this comparison involves two-dimensional averaging, the error is expected to be lower than in the previous comparisons because there is ample opportunity for the under- and overpredictions to cancel each other out.

Table 1: Total Eroded Mass During the Study Period.

	Per bucket	Total
Field study	17.21 kg	361.4 kg
Multiscale simulation	16.54 kg	347.3 kg
Relative error		3.9 %

4 Discussion and Conclusion

A precise estimation of the modeling error is hindered by the uncertain comparison between the simulations and the experiments. For test case 1, this uncertainty is caused by the fact that the simulated bucket is stationary and not geometrically equivalent to the experimental bucket. For test case 2, the uncertainty is driven by the experimental sediment load.

To estimate the modeling error, the simulation-experiment comparison uncertainty for test case 2 is quantified by propagating the standard deviations of the variables used to estimate the experimental sediment load by means of the Monte Carlo method. The standard deviation of the sediment concentration is estimated to be ±7%, whereas the standard deviation of the total discharge is estimated to be ±6.4 %, see Leguizamón et al. (2019) for the details. These values result in an uncertainty of the experimental sediment load of ±9.5%, which is the cause of the comparison uncertainty between simulation and experiment.

Taking the average over the 13 comparisons performed in Section 3.3.3, namely the erosion depth at 8 points, its average value along 4 sections, and the total eroded mass, the average relative error is equal to 26%. Considering the comparison uncertainty previously described, the multiscale modeling error for test case 2 is estimated to be 26% ± 10%.

The simulation of the erosion of a 2-D bucket reported in Leguizamón et al. (2018) shows that considering the surface modification caused by the process leads to an increase of the erosion rate of up to 45%. If this effect is included in the present case, the estimation of the multiscale modeling error would instead be equal to 28% ± 10%. Although the correction induces an overall increase of the predicted erosion, the fact that at some points it is underpredicted whereas at other points it is overpredicted with respect to the experiment explains the very slight increase of the average relative error.

For the first time it becomes possible to quantitatively predict the erosion process of an industrial-scale hydraulic turbine. This achievement was possible thanks to the use of a multiscale model that bridges the scale separation between the sediment impact dynamics and the turbulent sediment transport hydrodynamics. This approach bypasses the need for uncertain erosion correlations by relying on accurate simulations of the sediment impacts, taking into consideration the sediment shape and elasticity, and the high strain rate response of the base material by means of comprehensive physical models. Not only the model accurately predicts the erosion distribution on the bucket surface; it also brings information concerning the impact conditions and sediment flux against the wall which allows a better understanding of the erosion distribution results.

5 Outlook and Next Steps

Although the results presented in this report suggest that the proposed multiscale model of erosion is capable of predicting the erosion of prototype-scale Pelton turbines, there is still a number of open questions that need to be addressed.

The erosion results sensitivity to variations of the model inputs, including the material model parameters, the sediment sphericity and size distribution, should be investigated. By characterizing the model sensitivity to these inputs, a clear understanding of the most influential model parameters can be drawn; this understanding is key for the future practical application of the methodology.

Additional model validation test cases would provide a better estimation of the expected modeling error, and would highlight potential pitfalls. Yet again, a clear characterization of the model accuracy and limitations is fundamental for its future practical application.

An improvement that would render the multiscale model more attractive would be the inclusion of additional microscale material models to handle the case of hard-coated turbines. Given that the failure mechanism of this kind of coating is different from that of the base material, an alternative material model is in order; the Johnson-Holmquist constitutive and damage models are recommended.

By addressing these open questions, the applicability of the methodology will be considerably enhanced. Hopefully the multiscale model will then serve as a predictive tool whose insight might be included in the design process of Pelton turbines optimized for sediment-laden water, and in the management of Pelton turbine installations by estimating the sediment concentration threshold for economically reasonable preventive shut-off or in the scheduling of repair campaigns. This application would require an additional economic analysis including information such as the cost of replacing or refurbishing a runner, and the opportunity costs associated with not generating electricity during the preventive shut-off period and maintenance periods.

6 Publications

- Leguizamón, S., Jahanbakhsh, E., Alimirzazadeh, S., Maertens, A. & Avellan, F. (2019), “Multiscale simulation of the hydroabrasive erosion of a Pelton bucket: Bridging scales to improve the accuracy”, *International Journal of Turbomachinery, Propulsion and Power* 4, doi:10.3390/ijtpp4020009.
- Leguizamón, S., Alimirzazadeh, S., Jahanbakhsh, E., & Avellan, F. (2019), “Multiscale simulation of erosive wear in a prototype-scale Pelton runner”, *Submitted to Renewable Energy*.
- Sebastián Leguizamón (2019), “Multiscale Modeling and Simulation of Erosive Wear in Pelton Turbines”, EPFL Doctoral Thesis N°7115, doi:10.5075/epfl-thesis-7115.
- Siamak Alimirzazadeh (2019), "GPU-Accelerated Finite Volume Particle Simulation of Free Jet Deviation by Multi-jet Rotating Pelton Runner", EPFL Doctoral Thesis N° 7256 submitted.

7 References

- Alimirzazadeh, S., Jahanbakhsh, E., Maertens, A., Leguizamón, S. & Avellan, F. (2018), “GPU-accelerated 3-D finite volume particle method”, *Computers & Fluids* 171, 79–93, doi:10.1016/j.compfluid.2018.05.030.
- Alimirzazadeh, S., Kumashiro, T., Leguizamón, S., Maertens, A., Jahanbakhsh, E., Tani, K. & Avellan, F. (2018), “GPU-accelerated Pelton turbine simulation using finite volume particle method coupled with linear eddy viscosity models”, *Proceedings of the 29th IAHR Symposium on Hydraulic Machinery and Systems, IOP Conference Series: Earth and Environmental Science* 240, doi:10.1088/1755-1315/240/7/072018.
- Balu, P., Kong, F., Hamid, S. & Kovacevic, R. (2013), “Finite element modeling of solid particle erosion in AISI 4140 steel and nickel-tungsten carbide composite material produced by the laser-based power deposition process”, *Tribology International* 62, 18–28.
- Chitrakar, S., Neopane, H. & Gunnar, O. (2016), “Study of the simultaneous effects of secondary flow and sediment erosion in Francis turbines”, *Renewable Energy* 97, 881–889.
- Dehbi, A. (2008), “Turbulent particle dispersion in arbitrary wall-bounded geometries: A coupled CFD-Langevin-equation based approach”, *International Journal of Multiphase Flow* 34, 819–828.
- Felix, D., Abgottspon, A., Albayrak, I. & Boes, R. (2016), “Hydro-abrasive erosion on coated Pelton runners: Partial calibration of the IEC model based on measurements in HPP Fieschertal”, *Proceedings of the 28th IAHR Symposium on Hydraulic Machinery and Systems, IOP Conference Series: Earth and Environmental Science* 49, 122009.
- Finnie, I. (1960), “Erosion of surfaces by solid particles”, *Wear* 3, 87–103.
- Finnie, I. (1972), “Some observations on the erosion of ductile materials”, *Wear* 19, 81–90.
- Grein, H. & Schachenmann, A. (1992), “Solving problems of abrasion in hydroelectric machinery”, *Water Power and Dam Construction,* 19–24.
- Grewal, H. S., Singh, H. & Yoon, E. S. (2015), “Interplay between erodent concentration and impingement angle for erosion in dilute water-sand flows”, *Wear* 332, 1111–1119.

- Jahanbakhsh, E., Maertens, A., Quinlan, N., Vessaz, C. & Avellan, F. (2017), “Exact finite volume particle method with spherical-support kernels”, *Computer Methods in Applied Mechanics and Engineering* 317, 101–127.
- Jahanbakhsh, E., Vessaz, C., Maertens, A. & Avellan, F. (2016), “Development of a finite volume particle method for 3-D fluid flow simulations”, *Computer Methods in Applied Mechanics and Engineering* 298, 80–107.
- Johnson, G. R. & Cook, W. H. (1985), “Fracture characteristics of three metals subjected to various strains, strain rates, temperatures and pressures”, *Engineering Fracture Mechanics* 21, 31–48.
- Leguizamón, S., Jahanbakhsh, E., Maertens, A., Vessaz, C., Alimirzazadeh, S. & Avellan, F. (2016), “Impact erosion prediction using the finite volume particle method with improved constitutive models”, *Proceedings of the 28th IAHR Symposium on Hydraulic Machinery and Systems, IOP Conference Series: Earth and Environmental Science 49, 122010,* doi:10.1088/1755-1315/49/12/122010.
- Leguizamón, S., Jahanbakhsh, E., Maertens, A., Alimirzazadeh, S. & Avellan, F. (2017), “A multiscale model for sediment impact erosion simulation using the finite volume particle method”, *Wear* 392-393, 202–212, doi:10.1016/j.wear.2017.10.002.
- Leguizamón, S., Jahanbakhsh, E., Maertens, A., Alimirzazadeh, S. & Avellan, F. (2018), “Simulation of the hydroabrasive erosion of a bucket: A multiscale model with projective integration to circumvent the spatio-temporal scale separation”, *Proceedings of the 29th IAHR Symposium on Hydraulic Machinery and Systems, IOP Conference Series: Earth and Environmental Science* 240*,* doi:10.1088/1755-1315/240/7/072014.
- Leguizamón, S., Alimirzazadeh, S., Jahanbakhsh, E., & Avellan, F. (2019), “Multiscale simulation of erosive wear in a prototype-scale Pelton runner”, *Submitted to Renewable Energy*.
- Mann, B. & Arya, V. (2001), “Abrasive and erosive wear characteristics of plasma nitriding and HVOF coatings: their application in hydro turbines”, *Wear* 249, 354–360.
- Messa, G. V. & Malavasi, S. (2017), “The effect of sub-models and parametrizations in the simulation of abrasive jet impingement tests”, *Wear* 370-371, 59–72.
- Padhy, M. K. & Saini, R. P. (2012), “Study of silt erosion mechanism in Pelton turbine buckets”, *Energy* 39, 286–93.
- Perrig, A. (2007), “Hydrodynamics of the free surface flow in Pelton turbine buckets”, Ph.D. thesis, École Polytechnique Fédérale de Lausanne (EPFL N° 3715).
- Rai, A., Kumar, A. & Staubli, T. (2017), “Hydro-abrasive erosion in Pelton buckets: Classification and field study”, *Wear* 392-393, 8–20.
- Shewmon, P. & Sundararajan, G. (1983), “The erosion of metals”, *Annual Reviews of Materials* Science 13, 301–318.
- Takaffoli, M. & Papini, M. (2012), “Material deformation and removal due to single particle impacts on ductile materials using smoothed particle hydrodynamics”, *Wear* 274, 50–59.
- Vessaz, C., Jahanbakhsh, E. & Avellan, F. (2015), “Flow simulation of jet deviation by rotating Pelton buckets using finite volume particle method”, *Journal of Fluids Engineering* 137, 074501.
- Wang, M. H., Huang, C., Nandakumar, K., Minev, P., Luo, J. & Chiovelli, S. (2009), “Computational fluid dynamics modelling and experimental study of erosion in slurry jet flows”, *International Journal of Computational Fluid Dynamics* 23, 155–172.

- Wang, Y. F. & Yang, Z. G. (2008), “Finite element model of erosive wear on ductile and brittle materials”, *Wear* 265, 871–878.
- Wang, Y. F. & Yang, Z. G. (2009), “A coupled finite element and meshfree analysis of erosive wear”, *Tribology International* 42, 373–7.